Accepted version published in ACS Appl. Mater. Interfaces, 2022, 14, 46, 51910-51920; https://pubs.acs.org/doi/abs/10.1021/acsami.2c14929

# Spontaneous Formation of a Ligand-based 2D Capping Layer on the Surface of Quasi-2D Perovskite Films

Fei Zheng,[1,2] Thomas Raeber,[3] Sergey Rubanov,[4] Calvin Lee,[5] Aaron Seeber,[3] Christopher Hall,[1] Trevor A. Smith,[1] Mei Gao,[2] Dechan Angmo,[2*] Kenneth P. Ghiggino[1*]

[1] *School of Chemistry and ARC Centre of Excellence in Exciton Science, The University of Melbourne, Parkville, Victoria 3010, Australia*

[2] *Devices and Engineered Systems, CSIRO Manufacturing, Clayton, VIC 3168, Australia*

[3] *Materials Characterization and Modelling, CSIRO Manufacturing, Clayton, VIC 3168, Australia*

[4] *Ian Holmes Imaging Centre, Bio21 Institute, The University of Melbourne, Victoria 3010, Australia*

[5] *Bio21 Institute and School of Chemistry, University of Melbourne, Parkville, VIC 3010, Australia*

Email: Dechan.Angmo@csiro.au; ghiggino@unimelb.edu.au

## ABSTRACT:

Two-dimensional (2D) Ruddlesden-Popper phase perovskites (RPPs) are attracting growing attention for photovoltaic applications due to their enhanced stability compared to 3D perovskites. The superior tolerance of 2D RPPs films to moisture and oxygen is mainly attributed to the hydrophobic nature of the introduced long-chain spacer cations (ligands). In this work, it is revealed that a thin capping layer, consisting of self-assembled butylammonium ligands, is spontaneously formed on the top surface of quasi-2D perovskite film prepared by conventional one-step hot-casting. Based on morphological and crystallographic analysis of both the top/bottom surfaces and the interior of quasi-2D perovskite films, the formation process of the 2D capping layer and the assembly of RPPs, comprising both large and small slab thickness (large-*n*, small-*n*), is elucidated. The vertical orientation of RPPs that is required for sufficient charge transport for 2D perovskite solar cells (PSCs) is further verified. We propose that the surface capping layer is directly responsible for the long-term stability of 2D PSCs. This work provides detailed insight into the microstructure of quasi-2D RPPs films that should assist the development of strategies for unlocking the full potential of 2D perovskites for high-performance PSCs and other solid-state electronic devices.

KEYWORDS: Ruddlesden-Popper perovskite, capping layer, crystal orientation, stability, photovoltaic

# INTRODUCTION

Lead halide perovskites are a prominent candidate for expanding renewable energy uptake due to their extraordinary optoelectrical properties and potential for low-cost manufacturing of perovskite solar cells (PSCs).[1, 2] Conventional three-dimensional (3D) perovskites composed of lead-halide ($[PbI_6]^{4-}$) octahedra and organic cations (methylammonium or formamidinium, $MA^+/FA^+$) suffer instability issues caused by their strong interaction with moisture and oxygen from the ambient environment.[3, 4] To address this instability issue, quasi-two-dimensional (2D) perovskites with Ruddlesden-Popper phase (RPPs) offer enhanced stability and have been extensively explored to replace their 3D counterparts.[5-7] The general formula of RPPs can be described as $R_2A_{n-1}Pb_nI_{3n+1}$, wherein A is the small-size ammonium cations ($MA^+/FA^+$), R is the spacer cations with long alkyl or aromatic chains (butylammonium or phenethylammonium, $BA^+/PEA^+$), and *n* represents the number of $[PbI_6]^{4-}$ octahedral layers composing the inorganic slab that is sandwiched by two layers of $R^+$ cations.[8] The hydrophobicity and high dielectric constant of $R^+$ are responsible for the robustness of quasi-2D perovskites against phase segregation and ion migration, making them highly attractive for constructing PSCs with long-term stability under ambient operating conditions.[5, 7, 9-11]

The design strategies for 2D perovskites for photovoltaics fall into two categories. One is overlaying a horizontally aligned 2D perovskite (parallel to the substrate), with a slab thickness of $n$=1 or 2, on the surface of 3D perovskite by either spin-coating or solid-transfer methods to form a 2D/3D stacking structure.[12-15] This 2D protective capping layer can prevent oxygen and moisture from permeating into the 3D perovskite layer.[16] The other strategy is constructing the active layer entirely from the quasi-2D perovskites with a designated slab thickness of $\langle n \rangle$=4 or 5.[9, 17, 18] These films are generally composed of 2D perovskite slabs with various slab thicknesses ranging from small-$n$ ($n$=3, 4, 5) to large-$n$.[19] Due to the insulating nature of the spacer layers, charge transportation is believed to be confined within the 2D plane and hindered along the face-to-face direction.[20] Thus, the 2D capping layer coated on 3D perovskite films should be thin enough to allow charge tunnelling and the 2D RPPs slabs within quasi-2D perovskite films should be vertically oriented relative to the horizontal substrate to ensure sufficient charge transport and collection by top/bottom contacted electrodes.[7] Since the first success of PSCs based on quasi-2D $BA_2MA_{n-1}Pb_nI_{3n+1}$ ($\langle n \rangle$=4) RPPs achieved by the hot-casting method,[9] considerable efforts, including the compositional design of spacer cations,[21, 22] the incorporation of additives,[23] solvent engineering,[24] and optimisation of film casting methods have been made to achieve the vertical orientation of 2D RPPs slabs and thus improve the power conversion efficiency (PCE) of 2D PSCs from ~12% to ~20%,[25-27] which still lags behind those of mixed-cation mixed-halide 3D PSCs.[10] The construction of a 2D/3D bilayer structure combines the advantages of high stability brought by 2D RPPs, and the high PCE of 3D PSCs owing to the dominant composition of 3D perovskite forming the photo-active layers.[7] However, the conventional method for depositing ligands, which involves using a diluted ligand solution in isopropyl alcohol (IPA) and spin-casting at a very high speed, is not applicable for

slower deposition processes such as doctor blading or slot-die coating due to damage of the perovskite film by IPA,[28] and is thus not appropriate as a post-deposition strategy for large-scale fabrication.

2D PSCs based on the one-step deposited quasi-2D perovskite films are promising for achieving efficient and stable solar energy conversion for future commercialisation. Further improvement in the PCE of quasi-2D PSCs requires a better understanding of the film formation mechanism and microstructure correlated exciton/charge carrier dynamics.[29] Despite extensive investigations over the past five years, the phase distribution profile and the origin of the vertical orientation of 2D RPPs are not fully understood.[30] It is generally accepted that, during the conversion process from precursor solution to solid film on hot substrates, vertically oriented large-*n* 2D RPPs (3D-like) crystallise on the top surface due to fast solvent evaporation. These initial structures provide a template for the downwards vertical-oriented growth of 2D RPPs with decreasing slab thickness (*n*), leading to a sequential phase distribution of 2D RPPs from large-*n* (top) to small-*n* (bottom) along the vertical direction.[30] Lin *et al.* suggested that large-*n* RPPs form a continuous network throughout the films, acting as charge transport pathways for efficient 2D PSCs.[31] Zheng *et al.* recently found evidence for an alternative model in quasi-2D PSC films based on a sandwich-like structural model, consisting of a large-*n*/small-*n*/large-*n* phase arrangement, to describe the exciton dynamics for efficient 2D-PSCs.[32] All these models suggest the presence of vertically oriented large-*n*, or 3D-like, RPPs on the top surface of quasi-2D perovskite films should exhibit lower stability compared to the small-*n* or pure 2D (*n*=1) RPPs. This configuration seems inconsistent with the high operational stability achieved by quasi-2D PSCs, as large-*n* (3D-like) RPPs are less stable compared to the small-*n* RPPs.[33] In addition, the reason for the initial crystallisation of large-*n* RPPs from the top surface is also not well discussed. To address these discrepancies and uncertainty, a deeper investigation is required to reveal the microstructure and formation kinetics of quasi-2D perovskite films to guide further improvement in 2D PSCs.

In this work, the microstructure of quasi-2D perovskite films prepared by hot-casting was thoroughly investigated by morphological and crystallographic characterisations. The morphology of top/bottom surfaces and the interior of the quasi-2D film were studied by atomic force microscopy (AFM) and scanning electron microscopy (SEM) before and after the films were partially peeled by tape or totally peeled off from the substrate. Synchrotron-based grazing incidence wide-angle X-ray scattering (GI-WAXS) measurements of the quasi-2D film were carried out using both the top-side and bottom-side (peeled) detection to compare the different crystal orientation profiles of RPPs on the surfaces and in the film interior. It was found that the quasi-2D film interior is composed of vertically oriented RPPs with both small-*n* (*n*=3, 4, 5) and large-*n*, while the film surface is capped by a thin assembly layer of horizontally stacked BAI sheets. Based on these new findings, we propose that the spacer ligands-based surface capping layer is responsible for the long-term stability of 2D PSCs, while the vertically oriented large-*n*/small-*n* RPPs the high PCEs found in these systems.

## RESULTS AND DISCUSSION

In this work, $BA_2MA_{n-1}Pb_nI_{3n+1}$ (<*n*>=5) films prepared by hot-drop-casting were selected as prototypes to reveal the microstructure of quasi-2D RPP films that were utilised for 2D PSCs. Following the previous studies, these films are composed of a phase mixture of 2D RPPs with thicknesses that deviate from the designated <*n*>=5. Small-*n* (*n*=3, 4, 5) and large-*n* (*n*=L) RPPs were identified through the transient absorption (TA) spectra of the BA-based quasi-2D films. TA spectra obtained from the top-side (film/air interface) (**Figure 1A**) and bottom-side (film/substrate interface) excitation modes (**Figure S1**), appear as discrete ground-state bleaching (GB) peaks that correspond to the excitonic bandgaps of each 2D component.[32] The TA spectra recorded at 1 ps delay for both top- and bottom-side excitation are plotted in **Figure 1B**. By comparing the relative intensity of each peak, it can be deduced that more large-*n* (*n*=L) RPPs are located on the top side of the film while the bottom side is mainly occupied by small-*n* (*n*=3, 4, 5) RPPs components.[34] It should be noted that a small amount of *n*=2 RPPs is present at the bottom part of the film while the *n*=1 component is absent throughout the whole film.[35] The broad shape of the large-*n* GB peak implies there exists a distribution for these large *n* values, presumably ranging from the medium *n* to the maximum *n*.[32] We denote this set of RPPs as large-*n* for simplicity. Analysis of the dynamics (**Figure 1C**) shows a gradual increase of the large-*n* GB amplitude which is coincident with an amplitude decrease of small-*n* peaks, which is indicative of exciton funnelling from the small-*n* 2D RPPs to the large-*n* components. This funnelling process is supported by photoluminescence (PL) measurements made on both sides of the film, where it is observed that the PL from large-*n* RPPs dominates (**Figure 1D**). The identical PL peak position implies emission originates from the same phase domains of large-*n* RPPs, possessing the maximum *n* value and thus the lowest band-gap. The maximum *n* can be obtained by Equation-1:[23]

$$E_x = \frac{h \cdot c}{e \cdot \lambda_{PL}} = 1.623\ eV + \frac{1\ eV}{0.063 \cdot n^2 + 0.458 \cdot n + 0.811} \quad (1)$$

wherein $E_x$ denotes the excitonic gap of the RPPs component with slab thickness *n* that can be calculated from the corresponding PL peak position ($\lambda_{PL}$). The maximum *n* corresponding to ~754 nm PL emission can thus be estimated as *n*=23.

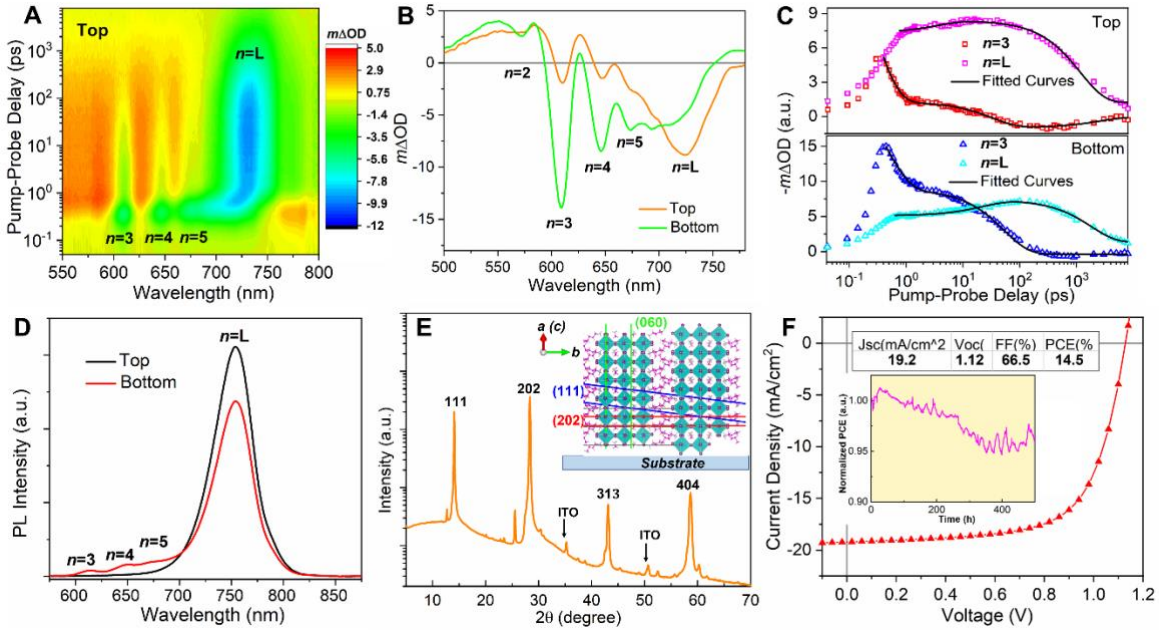


**Figure 1** (**A**) Pseudo-colour 2D plot of the TA spectrum ($m\Delta$OD) of the $BA_2MA_{n-1}Pb_nI_{3n+1}$ (<$n$>=5) quasi-2D perovskite film obtained by top-side excitation and transmission detection; (**B**) TA spectra as a function of probe wavelength at pump-probe delays of 1 ps recorded under both top-side and bottom-side excitation modes; (**C**) Time decay profiles of GB peaks corresponding to small-$n$ ($n$=3) and large-$n$ ($n$=L) RPPs obtained from the top-side (upper panel) and bottom-side (lower panel) excitation and transmitted detection; (**D**) PL spectra of $BA_2MA_{n-1}Pb_nI_{3n+1}$ (<$n$>=5) film measured by top-/bottom-side excitation and reflection detection; (**E**) XRD pattern of the $BA_2MA_{n-1}Pb_nI_{3n+1}$ (<$n$>=5) film deposited on a PEDOT/ITO substrate. The inset schematically shows the arrangement of specific lattice planes within the [101] oriented $n$=3 RPPs crystal domains; (**F**) $J$-$V$ curves of 2D PSCs based on the hot-cast $BA_2MA_{n-1}Pb_nI_{3n+1}$ (<$n$>=5) film and the corresponding PCE tracking for device stability testing.

The overall crystal orientation profiles of the $BA_2MA_{n-1}Pb_nI_{3n+1}$ (<$n$>=5) quasi-2D film were probed using an X-ray diffractometer under the Bragg-Brentano (BB) mode, which collects diffraction signals along the out-of-plane (OP) direction of the film. **Figure 1E** shows the XRD patterns measured from the top surface of the quasi-2D perovskite film deposited on a glass substrate by hot-casting, which features prominent diffraction peaks at 2θ=14.03° and 28.31°. These peaks are indexed as (111) and (202) diffraction peaks that originated from the corresponding lattice planes of the vertically oriented 2D RPPs slabs.[36] As schematically illustrated in the inset of **Figure 1E**, 2D RPPs with $n$=3, for example, are composed of three layers of $[PbI_6]^{4-}$ octahedral sheets sandwiched by two layers of $BA^+$ spacer cations along the 2D stacking direction ($\vec{b}$ axis).[8] The vertical orientation (<101> normal to the substrate) of this 2D crystal structure makes the (111) and (202) lattice plane nearly parallel to the substrate, thus leading to strong (111) and (202) XRD peaks collected in the out-of-plane (OP) direction under the BB mode. If the 2D RPPs slabs were horizontally oriented (<010> normal to the substrate), the (0$k$0) reflection peaks, e.g. (060), would be observed instead. According to the general crystal structure of RPPs, the positions of the (111) and (202) peaks are almost independent of the slab thickness with $n$>2. Thus, the XRD pattern obtained here featuring the dominant (111) and (202) peaks and the absence of (0$k$0) peaks implies all RPPs (various $n$) within the quasi-2D film are vertically oriented relative to the

horizontal substrate. Based on the efficient exciton funnelling process occurring and the vertical orientation profile of 2D RPPs within the quasi-2D films, the high photovoltaic performance of these films would be expected. **Figure 1F** presents the *J-V* curves of 2D PSCs with the structure of ITO Glass/PEDOT: PSS/Quasi-2D Perovskite/PCBM/PEIE/Ag based on these hot-cast $BA_2MA_{n-1}Pb_nI_{3n+1}$ (<*n*>=5) films, showing a champion PCE of ~14.5% (performance parameter listed in the inset), which is among the highest value reported for this 2D recipe. The inset of **Figure 1F** also shows the stability testing result of these 2D PSCs. The encapsulated cells in air retained >96% of their initial PCE after 500 hours under constant AM1.5G solar illumination, demonstrating the excellent performance stability of these 2D PSCs.

The surface morphology of the $BA_2MA_{n-1}Pb_nI_{3n+1}$ (<*n*>=5) quasi-2D perovskite film was characterised by high-resolution AFM. To reproduce the actual film formation conditions utilised in fabricating 2D PSCs, the films were hot-cast on the PEDOT: PSS (hole transporting layer) coated ITO substrates. **Figure 2A** presents an AFM image detailing the top surface of the film. Perovskite grains with a lateral size of ~1-2 μm compose the film, featuring either with or without sunken pits in the grain centre. A previous study has been shown that, grains without pits possess a higher composition of large-*n* 2D RPPs when compared to those with pits and form Brownian tree patterns by diffusion-limited-aggregation (DLA).[37] The magnified AFM image (**Figure 2B**) shows the film surface is constructed of horizontally oriented semi-round 2D sheets stacked consecutively. Height profile analysis cutting across individual sheets is presented in the inset, showing the thickness of the sheets on the surface is approximately 0.8 nm. This thickness estimate is further confirmed by additional height analyses performed on two other sites as shown in **Figure S2**. Based on the crystal structure of $BA_2PbI_4$ (*n*=1) RPP (upper panel, **Figure 2C**), the theoretical thickness of the *n*=1 2D perovskite sheet is 1.34 nm, which has already been verified by the experimental observation.[38, 39] Thus, the mono-sheets observed here are excluded from being $BA_2PbI_4$ (*n*=1) 2D RPPs owing to the large disagreement in thickness. This is consistent with the TA spectra (**Figure 1B**) and XRD pattern (**Figure 1E**), which also suggest the absence of a *n*=1 RPP component within the quasi-2D perovskite film. Alternatively, the combined thickness of two spacer cations ($BA^+$) sandwiching the $[PbI_6]^{4-}$ octahedral layer, which is ~0.7 nm, approximates the thickness of the mono-sheets (~0.8 nm), implying they can be bilayers of butylammonium iodide (BAI). As depicted in the lower panel of **Figure 2C**, two layers of self-assembled BAI molecules connect head-to-head, forming a 2D sheet predominantly comprised of spacer ligands, which is different to the 2D perovskite bilayer reported in previous post passivation strategies.[13] This bilayer molecular structure generally appears for Langmuir-Blodgett (LB) bilayers of amphiphile molecules,[40] such as tetrabutylammonium iodide (TBAI).[41] Considering the amphiphilic property of the BAI, the formation of self-assembled BAI bilayer sheets initiated from the solvent/air interface is reasonable. Thus, the horizontally stacked sheets on the top surface of quasi-2D perovskite films can be assigned to BAI bilayer sheets spontaneously formed during the film casting process. The

self-assembly of BAI sheets proposed here is supported in part by a recent publication which suggests the existence of spacer cations (3-fluoro-phenylmethyl ammonium, 3FBA+) on the top surface of as-prepared quasi-2D perovskite films.[27] This observation is different to the previous structural and film formation models suggesting the occupation of large-*n* (3D-like) RPPs on the top surface of quasi-2D perovskite films. On the contrary, this proposed configuration resembles the 2D/3D bilayer structure constructed *via* post-deposition for improving the stability of 3D PSCs.[13, 14, 16]

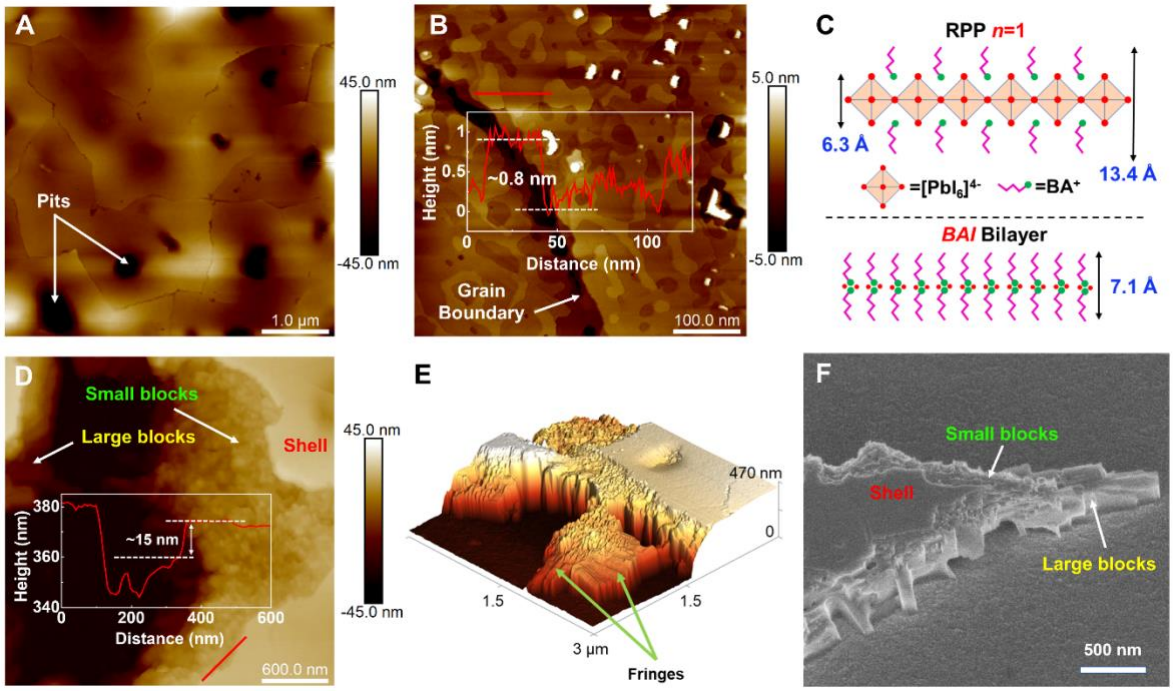


**Figure 2** AFM images showing the morphology of the top surface of the $BA_2MA_{n-1}Pb_nI_{3n+1}$ (<*n*>=5) film deposited on PEDOT/ITO substrate for a moderate (**A**) and a small (**B**) area. The inset in (B) shows the height profile traced along the red line marked in the figure; (**C**) Schematic illustration of the structures of $BA_2PbI_4$ (*n*=1) RPPs individual sheet and the BAI bilayer; (**D**) AFM image of the peeling edge of partially peeled $BA_2MA_{n-1}Pb_nI_{3n+1}$ (<*n*>=5) film deposited on PEDOT/ITO substrate; (**E**) 3D-view AFM image of the peeling edge obtained from the other site; (**F**) SEM image of the partially peeled quasi-2D perovskite film focusing on the peeling edge.

To explore the impact of BAI capping layer on the assembly behaviour of 2D RPPs deep inside the quasi-2D perovskite films, scotch tape was used to partially peel the films from the top side to obtain the peeling edges. These are the boundaries between the areas of un-peeled film and bare substrate, as denoted in **Figure S3**. The AFM topographic image given in **Figure 2D** features the un-peeled film surface, the peeling edge, and the PEDOT/ITO substrate. The surface of the film appears as a compact and layered shell, which is in distinct contrast to the film interior structure, as the latter exhibits small and large blocks from top to bottom. Based on the analysis of **Figure 2B&C**, the shell should be composed of horizontally stacked BAI sheets. Its overall thickness estimated from height profile analysis is up to ~15 nm, which is quite thin relative to the whole film thickness (~350 nm). As indicated by the TA and PL spectra from the top and bottom sides (**Figure 1**), more large-*n* RPPs occupy the top side, and the small-*n* (*n*=3, 4, 5) RPPs tend to dominate the bottom side of the films. Thus, it can be

inferred that the vast number of small-sized blocks directly beneath the shell are large-*n* RPPs, and the large blocks at the bottom side of the films are small-*n* (*n*=3, 4, 5) RPPs. The 3D-view AFM image of the peeling edge at the other point shown in **Figure 2E** directly demonstrates the hierarchical distribution of these components along the vertical direction. Notably, the edges of 2D RPPs crystal slabs, which are featured as parallel fringes, appear on the surface of the large blocks along the out-of-plane direction. This observation indicates these large blocks located at the film bottom are assembled from the vertically oriented (edge-on) small-n 2D RPPs slabs. The remarkable contrast between the ligand-based shell, large-*n* and small-*n* 2D RPPs comprising the quasi-2D film was also verified through scanning electron microscopy (SEM). **Figure 2F** presents the SEM image, with a tilt angle of 40°, of the partially peeled quasi-2D perovskite film obtained in the secondary electron detection mode. The compact shell on the film surface can be easily identified, beneath which are small blocks and large blocks. The cliff-like appearance of large blocks at the bottom part of the film is another sign of the vertical orientation profiles adopted by the small-*n* RPPs slabs. The compact shell comprised of horizontally stacked BAI sheets is confirmed, which is ideal for protecting the film interior from the ambient environment as these ligands themselves are the origin of the superior stability of 2D RPPs. Therefore, we propose the spacer ligand-based 2D capping layer is responsible for the long-term stability of 2D PSCs based on this quasi-2D film (**Figure 1F**).

Although the morphology of quasi-2D perovskite films has been widely investigated by ourselves and others, the direct characterisation of the buried (bottom) surface has not been reported to date. To directly assess the bottom surface of the hot-cast $BA_2MA_{n-1}Pb_nI_{3n+1}$ (<*n*>=5) film by AFM and SEM characterisations, an epoxy glue-assisted peeling method was applied to peel off the quasi-2D film from the substrate fully.[42] As schematically illustrated in **Figure 3A**, a drop of pre-mixed epoxy glue was dropped on the top surface of the quasi-2D film, followed by coverage with another clean glass substrate. The two glass substrates were clipped together by a metal clip for 1 hour and then separated by hand. Through this process, the quasi-2D perovskite film was then peeled off from the old substrate and adhered to the new substrate by the solidified epoxy glue, exposing the previously bottom surface of the quasi-2D film. The AFM image in **Figure 3B** shows the morphology of the bottom surface of the freshly peeled $BA_2MA_{n-1}Pb_nI_{3n+1}$ (<*n*>=5) film, featuring a flat surface decorated by some scattered small flakes. As far as we know, the bottom surface of the quasi-2D film should emerge as the edges of the vertically oriented small-*n* (*n*=3, 4, 5) RPPs slabs, which is further confirmed by the appearance of fringes in the AFM images. Height profile analysis (inset of **Figure 3B**) shows the ribbon-like small flakes "floating" on the film surface possessing a thickness of around 20 nm. Considering the compact adhering of the quasi-2D perovskite film on the substrate, the appearance of these isolated flakes contrasts with the expected flat bottom surface of the film. We suspect these small flakes are formed by the recrystallisation of the edges of the 2D RPPs that occurs straight after the film is peeled off. This is supported by the AFM characterisation of the peeled film that is exposed to air for one day in the air,

which is full of small flakes (**Figure 3C**). When the exposure time is prolonged for one week, both the quantity and the size of the small flakes are significantly increased (**Figure S4A**). This observation suggests that the 2D RPPs with edges exposed to air are quite unstable and tend to recrystallise to other configurations with time. In comparison, as depicted in **Figure S4B**, the AFM image of the top surface of the quasi-2D perovskite films exposed to air for one week shows no obvious change in morphology relative to the fresh sample (**Figure 2A**). Thus, it can be deduced that the ligand-based 2D capping layer spontaneously formed on the top of vertically oriented 2D RPPs can prevent the unexpected recrystallisation process that may harm the stability and efficiency of 2D PSCs.

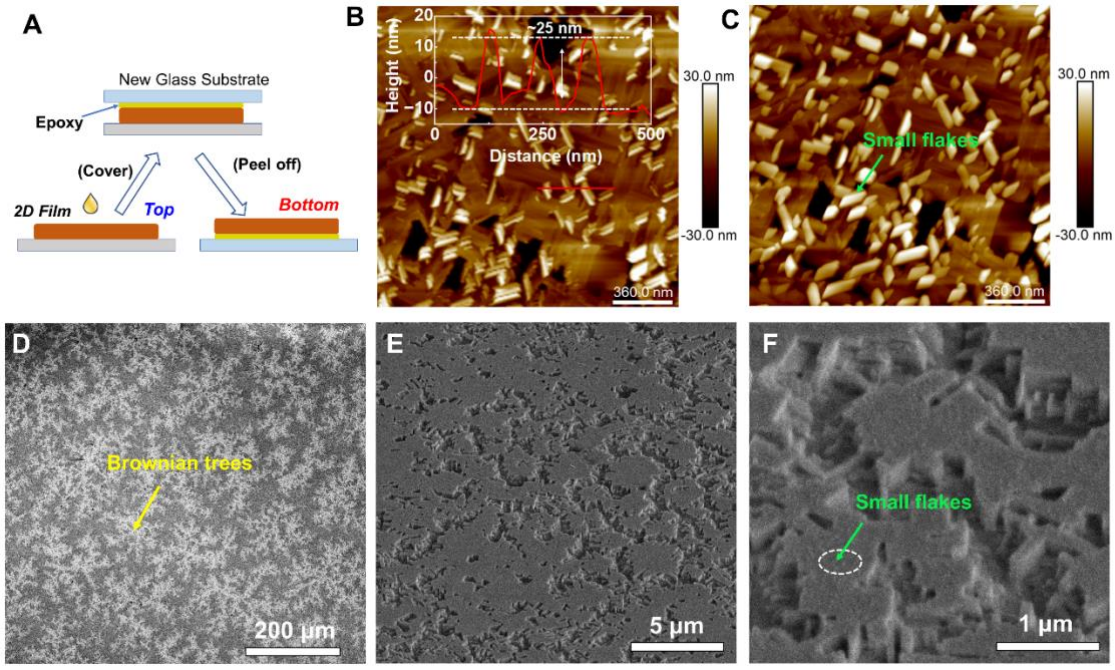


**Figure 3** (**A**) Schematic of the process for peeling off the quasi-2D perovskite films from a substrate using epoxy glue; AFM images of the bottom surface morphology of the $BA_2MA_{n-1}Pb_nI_{3n+1}$ (<*n*>=5) quasi-2D films right after peeling (**B**) and exposed to air for one day (**C**); (**D&E&F**) SEM images of the bottom surface of the quasi-2D film with gradually increasing magnification.

The morphology of the bottom surface of the quasi-2D film is further explored by SEM. **Figure 3D** presents the SEM top-view image of the freshly peeled $BA_2MA_{n-1}Pb_nI_{3n+1}$ (<*n*>=5) film with low magnification. The strong contrast of bright Brownian tree dendrites is clearly apparent, which matches well with those patterns that appear in the optical transmission image (**Figure S5**). According to our previous report,[37] these Brownian trees are formed by diffusion-limited-aggregation of MA-rich 2D RPPs phase domains that first crystallised out from the solution. By increasing the magnification (**Figure 3E**), the Brownian trees are tracked to be the film area with voids and edges, whereas the dark background regions are the flattened areas of the bottom surface. It is demonstrated that these voids are accompanied by the separated (small-*n*) large blocks at the bottom side of the film. Chen *et al.* recently proposed that voids appearing in the buried interface of 3D perovskite films are induced by the trapping of solvent as the film crystallisation direction is from top to bottom.[43] Thus, the preferential appearance

of voids under the bottom surface of quasi-2D perovskite film areas featured with Brownian trees indicates the top-to-bottom crystallisation tendency for RPPs is more prominent in these areas compared to the rest. This interpretation agrees well with the previous assumption that the perovskite grains constructing the Brownian trees are first crystallised out from the solution, with the fast formation more likely causing the trapping of the solvent at the bottom during the film formation process. An enlarged SEM view of the region of the Brownian tree is presented in **Figure 3F**, from which the perovskite grains can be identified. The orientations of the large blocks within each grain are coordinated, with the long axes either parallel or perpendicular to each other, and differing from those of the neighbours, indicating the independent crystallisation of each grain. Small flakes adhering to the surface of large blocks and flat film areas are also observed in the SEM image as sharp needles, which is consistent with the AFM characterisation result.

Grazing incidence wide-angle X-ray scattering (GIWAXS) is a powerful technique to assess the crystallographic arrangement of solid polycrystalline materials. Herein, the crystal orientation and phase distribution profiles of 2D RPPs within the hot-cast $BA_2MA_{n-1}Pb_nI_{3n+1}$ (<*n*>=5) quasi-2D perovskite film were systematically investigated by angle-dependent GI-WAXS. To consolidate the interpretation of these experimental results, simulation of GIWAXS patterns for large-*n* and small-*n* RPPs was performed.[44] Due to the lack of crystallographic analysis for large-*n* 2D RPPs in the literature, the crystal parameters of $MAPbI_3$ with a tetragonal phase was adopted instead to approximate the GI-WAXS pattern of large-*n* (3D-like) $BA_2MA_{n-1}Pb_nI_{3n+1}$ considering their structural similarity. As reported,[8] 2D RPPs with (*n*>1) are structurally derived by cutting the $MAPbI_3$ perovskite along the (110) lattice plane and decorating the two surfaces with BA cations. Thus the <110> and <$\bar{1}$10> orientation of the $MAPbI_3$ crystal normal to the substrate can represent the horizontal and vertical alignment of large-*n* 2D RPPs slabs. The crystal symmetry of these two directions leads to the identical appearance of simulated GI-WAXS patterns (**Figure S6**).[45] For small-*n* 2D RPPs, $BA_2MA_2Pb_3I_{10}$ (*n*=3) was selected for the GI-WAXS pattern simulation. In contrast to the large-*n* RPPs, the GI-WAXS patterns of the <010> horizontally (<010> direction normal to the substrate) and vertically (<101> normal to the substrate) oriented small-*n* RPPs films are quite different to each other. As shown in **Figure 4A&4B**, the reflection peaks are associated with the stacking direction ($\vec{b}$) of 2D RPPs, e.g. (0*k*0), (1*k*1) and (2*k*2), are mainly linearly arranged along the out-of-plane (OP) direction at $q_{xy} = 0\ \text{Å}^{-1}, 1.0\ \text{Å}^{-1}, 2.0\ \text{Å}^{-1}$ for the horizontally oriented 2D slabs and along the in-plane (IP) direction at $q_z = 0\ \text{Å}^{-1}, 1.0\ \text{Å}^{-1}, 2.0\ \text{Å}^{-1}$ for the vertical ones. **Figure 4C** plots the X-ray scattering intensity profile of the simulated GI-WAXS of vertically oriented *n*=3 RPPs film along $q_z = 0\ \text{Å}^{-1}, 1.0\ \text{Å}^{-1}, 2.0\ \text{Å}^{-1}$. The discrete reflection peaks within the $0\ \text{Å}^{-1} \sim 1.0\ \text{Å}^{-1}$ range for $q_{xy}$ can reasonably be assigned to the vertically (<101>) oriented *n*=3 2D slabs viewing from the <$\bar{1}$01> direction. These peaks are all perfect indicators for the *n* values of small-*n* 2D RPPs. Strong diffraction peaks indexed as 10$\bar{1}$, 200, 311, 400,

etc., are assigned to diffraction from vertically (<101>) oriented 2D slabs viewing from the <010> direction.

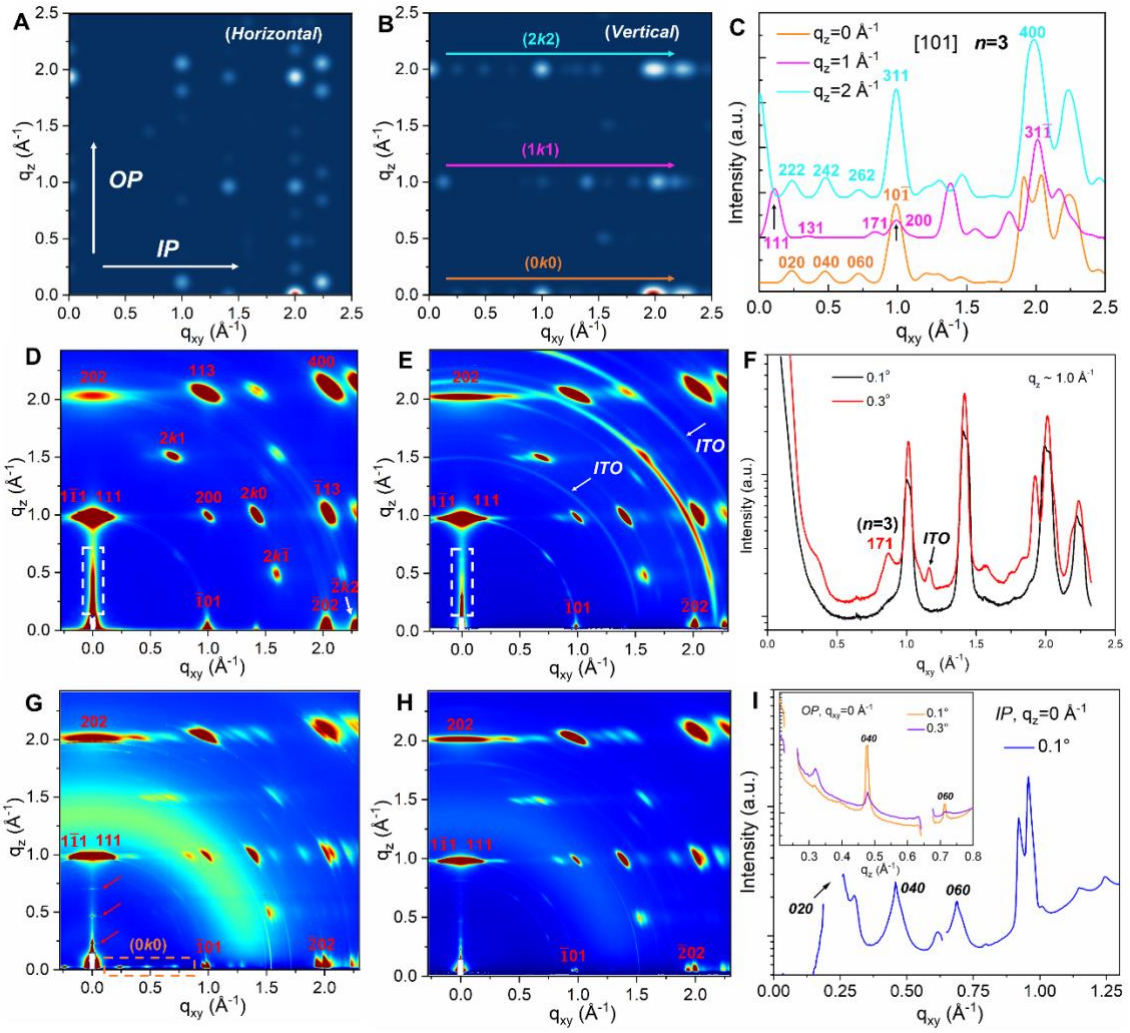


**Figure 4** Simulated GI-WAXS patterns of pure *n*=3 RPPs film with (**A**) horizontal (<010>) and (**B**) vertical (<101>) crystal orientation; (**C**) Scattering intensity profiles of (B) integrated along $q_z \sim 0\ \text{Å}^{-1}, 1.0\ \text{Å}^{-1}, 2.0\ \text{Å}^{-1}$; Indexed GI-WAXS patterns of $BA_2MA_{n-1}Pb_nI_{3n+1}$ (<*n*>=5) film measured from the top surface with an X-ray incidence angle of 0.1° (**D**) and 0.3° (**E**), and the corresponding intensity profiles integrated along $q_z \sim 1.0\ \text{Å}^{-1}$ (**F**); GI-WAXS patterns of the epoxy-peeled $BA_2MA_{n-1}Pb_nI_{3n+1}$ (<*n*>=5) film (bottom surface) with an X-ray incidence angle of 0.1° (**G**) and 0.3° (**H**); (**I**) Scattering intensity profile of (G) integrated along the *IP* ($q_z = 0\ \text{Å}^{-1}$) direction. The inset shows the comparison of the scattering profile for (G) and (H) integrated along the *OP* ($q_{xy} = 0\ \text{Å}^{-1}$) direction.

The 2D GIWAXS patterns of the quasi-2D perovskite film (top surface) deposited on PEDOT/ITO glass substrate and peeled film (bottom surface) attached on epoxy/glass at an incident angle of 0.1° and 0.3° are shown in **Figure 4D, E, G, H**, respectively. 0.1° is smaller than the critical angle for total external reflection of the X-ray beam on the surface of the quasi-2D film, leading to the shallow detection depth of GI-WAXS at this angle. Thus, the GI-WAXS pattern shown in **Figure 4D** and **Figure 4G** mostly reflects the crystallinity of the top and bottom parts of the film, respectively. The presence of scattering rings belonging to the ITO substrate, as marked in **Figure 4E**, confirms the X-ray can

detect the whole film with the 0.3° incidence angle. The GI-WAXS pattern present in **Figure 4D** closely resembles the simulated pattern of the textured 3D $MAPbI_3$ film (**Figure S4**), suggesting the top part of the quasi-2D film is composed of large-*n* RPPs. Although it is difficult to judge the crystal orientation profile of large-*n* RPPs through these discrete scattering spots, the obvious horizontal stretching of the (202) peak along the IP direction indicates the large-*n* RPPs are vertically oriented. By increasing the X-ray penetration depth at an incident angle of 0.3° (**Figure 4E**), several discrete reflections along $q_z = 1.0$ $Å^{-1}$and 2.0 $Å^{-1}$ associated with vertically-oriented small-*n* RPPs (**Figure 4b**) increase in intensity relative to **Figure 4D**. This suggests a higher proportion of small-*n* RPPs in the film bulk relative to the surface. The linecut along $q_z = 1.0$ $Å^{-1}$ (**Figure 4F**) demonstrate the increase in intensity of the 171 peaks corresponding to the vertically oriented *n*=3 RPPs component upon the increase of X-ray incidence angle from 0.1° to 0.3°. The missing (0*k*0) reflection spots along the $q_{xy}$ axis (IP direction, $q_z = 0$ $Å^{-1}$) is consistent with the literature, which may result from the obscuring of scattering signal from the bottom side by the sample horizon.[46]

The bottom surface of the quasi-2D film peeled by epoxy detected with a 0.1° X-ray incidence angle exhibits a scattering pattern with prominent features that match those of the vertically-oriented small-*n* RPPs from vertically oriented small-*n* RPPs. Of particular note in **Figure 4G** are the distinct (0*k*0) scattering features along the $q_{xy}$ axis (IP direction), which correspond to the 020, 040 and 060 reflections in the simulated vertically-oriented *n*=3 RPPs (**Figure 4B**). That these scattering features are much more apparent in **Figure 4G** than **Figure 4E** suggests that these vertically-oriented *n*=3 RPPs comprise significant portions of the bottom part of the film. Notably, these peaks are also appearing along the $q_z$ axis (OP direction), featuring sharper radial width and lower intensity compared to those along the $q_{xy}$ axis. Based on the observations of small flakes at the bottom surface by AFM, we speculate these (0*k*0) reflection peaks (*n*=3) appearing along the $q_z$ axis is attributed to the small flakes composed of horizontally oriented *n*=3 RPPs. This assumption is strengthened by the significant decrease in intensity of these OP (0*k*0) reflections at an incidence angle of 0.3° as shown in **Figure 4H** and the inset in **Figure 4I**, which in turn suggests that these horizontally-oriented *n*=3 RPPs are predominantly confined to the bottom few nanometers of the film. As we have concluded based on AFM characterisation, this small amount of horizontally oriented *n*=3 RPPs small flakes is formed by recrystallisation after the peeling process. The expected improved crystallinity and structural regularity of this component are consistent with the sharp appearance of these reflection peaks presented in the GI-WAXS pattern. Therefore, it can be confirmed that the bottom part of the hot-cast $BA_2MA_{n-1}Pb_nI_{3n+1}$ (<*n*>=5) quasi-2D film is predominantly composed of small-*n* (*n*=3) RPPs, which are vertically oriented (<101> textured). The transition of the crystal orientation at the bottom surface also suggests the vertically oriented 2D RPPs, especially the slab edges, are not stable.

The existence of BAI sheets on the top surface of the quasi-2D perovskite film is also suggested by GI-WAXS characterisation. As shown in **Figure 4D, E**, a prominent and long-range distributed Yoneda streak (labelled by a white rectangle) appeared in the $q_z$ axis ($q_{xy}$=0 $Å^{-1}$) of GI-WAXS patterns collected from the top surface of the $BA_2MA_{n-1}Pb_nI_{3n+1}$ (<*n*>=5) film. This phenomenon can be observed in the literature, where an analogous Yoneda streak was only present in scattering patterns corresponding to perovskite films with $BA^+$ ligands present.[47] By comparison, as shown in **Figure 4G, H**, the Yoneda peak almost disappears in the GI-WAXS pattern collected from the bottom surface of the quasi-2D film, wherein the BAI capping layer is absent. In addition, as shown in **Figure S7**, the GI-WAXS pattern for the $MAPbI_3$ film (free of BA cations) does not feature this type of Yoneda streak. According to literature, a Yoneda streak in a GI-WAXS pattern is sensitive to the scattering layers, such as chemical surface layers, on the film surface.[48] Thus, we propose the strong Yoneda streak observed for the GI-WAXS patterns of quasi-2D perovskite films is associated with the dynamic scattering of the horizontally packed BAI sheets. The GI-WAXS results in this work would support the existence of BAI sheets on the top surface of the quasi-2D perovskite films.

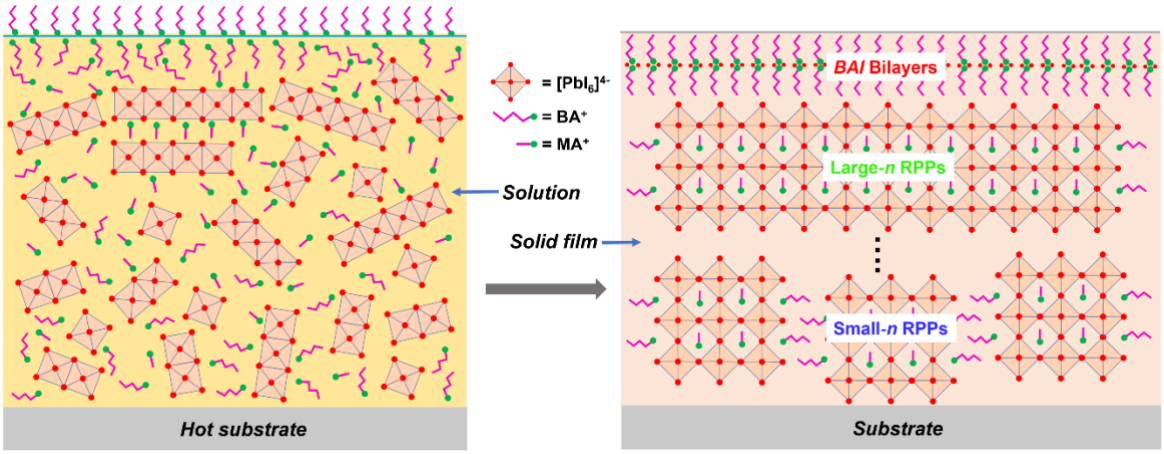


**Figure 5**. Schematic illustration for the formation of a ligand-based capping layer on the surface and the hierarchical assembly of RPPs within hot-cast quasi-2D perovskite films.

In summary, the phase distribution and crystal orientation profiles of the hot-cast $BA_2MA_{n-1}Pb_nI_{3n+1}$ (<*n*>=5) quasi-2D films for application in PSCs were explored in depth by directly collecting morphological and crystallographic information from the interior and buried interface of the film, leading to the establishment of a new structural model featuring the presence of a thin capping layer composed of horizontally oriented 2D BAI sheets. The formation mechanism of this specific quasi-2D perovskite film structure can be proposed as follows (**Figure 5**). After dropping precursor solution onto a hot substrate, the fast evaporation of solvent leads to supersaturation. Owing to the hydrophobicity of the alkyl chains, butylammonium cations ($BA^+$) at the liquid/air interface tend to self-assemble with the butyl chains' direction oriented to air to reduce the surface energy, analogous to the formation of Langmuir-Blodgett (LB) monolayers reported for tetrabutylammonium ($TBA^+$).[40] The tendency of $BA^+$ moving towards the interface and the evaporation of solvent leads to the enrichment and high

concentration of $BA^+$ cations at the top layer of the solution, which then self-assemble into $BA^+$ monolayers. With the further evaporation of solvent, these monolayers combined into bilayers with head-to-head orientation and connected by $I^-$ anions to form 2D BAI sheets. The formation of these ligand-based sheets substantially consumes $BA^+$, inevitably leading to the local depletion of the spacer cations in the precursor and thus facilitating the formation of MA-rich intermediate phases that crystallise into large-*n* (*n*~23) RPPs. The vertical orientation of the large-*n* RPPs growing independently beneath the horizontal-oriented 2D BAI sheets can be attributed to their intrinsic <101> crystal orientation preference on flat surfaces as reported before.[49] Along with the formation of large-*n* RPPs downwards, the concentration of $BA^+$ in the remaining solution gradually increases, leading to templated growth of 2D RPPs with gradually decreased slab thickness. Ultimately, large blocks composed of vertically oriented small-*n* (*n*=3) RPPs are formed and dominate the bottom part of the film. This hierarchical arrangement of 2D capping layer (BAI)/small blocks (large-*n* RPPs)/large blocks (small-*n* RPPs) in the vertical direction applies over the whole film, despite the presence of Brownian tree-shaped dendrites in the quasi-2D film. The only difference in phase construction between the Brownian trees and non-dendritic film areas lies in perovskite grains aggregated into Brownian trees containing more large-*n* RPPs and are accompanied by many empty voids at the bottom side caused by faster crystallisation compared to grains in the rest of the film. Based on the above discussion, the precise control of the thickness of the 2D BAI capping layer formed on the top surface and the elimination of the voids present at the buried interface of quasi-2D perovskite films would be important for further development of efficient 2D-PSCs.

## CONCLUSIONS

In conclusion, the crystal orientation and phase distribution profiles of RPPs within the quasi-2D Ruddlesden-Popper perovskite films for efficient and stable 2D PSCs were comprehensively investigated. The spontaneous formation of a horizontally oriented BAI-based 2D capping layer, appearing as a compact shell, on the top surface of quasi-2D $BA_2MA_{n-1}Pb_nI_{3n+1}$ (<*n*>=5) film prepared by one-step hot-casting was revealed. Beneath this shell, small blocks composed of large-*n* RPPs, and large blocks composed of small-*n* RPPs, which are all vertically oriented, occupy the top and bottom part of the film, respectively. Compared to the recrystallisation of *n*=3 RPPs at the bottom surface after peeling, the front surface capped by the horizontally oriented BAI stacking sheets is quite stable, implying the superior stability of 2D PSCs is attributed to this 2D capping layer, analogous to the scenario of 2D/3D bilayer structures. Implementing precise control of the 2D capping layer formed on the surface of quasi-2D perovskite films should be advantageous for improved efficiency and stability of 2D PSCs in future studies. Our results also provide new insights into the formation mechanism of quasi-2D perovskite films based on the hierarchical assembling of 2D RPPs with vertical orientation. The outcomes of this work provide a deeper understanding of film structure required for improved

design strategies to unlock the full potential of 2D perovskites for high-performance 2D PSCs and other solid-state optoelectronic devices.

# EXPERIMENTAL SECTION

### 1. Preparation of Quasi-2D perovskite films and solar cells

*Film preparation*: Lead iodide ($PbI_2$, 0.6 mmol), methylammonium iodide (MAI, 0.48 mmol), and *n*-butylammonium iodide (BAI, 0.24 mmol) were dissolved into 2 ml anhydrous dimethylformamide (DMF) with magnetic stirring at 70 °C for 1 hour. After cooling this solution to room temperature (RT), 2.0 mg methylammonium chloride (MACl) was added, followed by stirring at RT for 1 hour to obtain a 0.3 M (in $Pb^{2+}$) precursor solution of $BA_2MA_{n-1}Pb_nI_{3n+1}$ (<*n*>=5) perovskite doped with 6 mol% MACl. The aqueous solution of PEDOT: PSS was spun onto cleaned and UV ozone-treated ITO glass (25×25×0.7 mm, ~10 Ohm/Sq) or bare glass at 5000 rpm, followed by annealing at 140 °C for 20 mins to prepare the PEDOT/ITO glass or PEDOT/glass substrates for the deposition of quasi-2D perovskite films. 5 µL of precursor was dropped onto the centre of the substrate, which was placed on a 60 °C hot plate to form a circular film after the spreading and evaporation of DMF. The film was then transferred to a 100 °C hot plate for 2 minutes of annealing.

*Device Fabrication and Characterisation*: For the fabrication of 2D PSCs, PCBM (10 mg/ml in $CHCl_3$) and PEIE (0.05% w/w in isopropanol) solution were subsequentially spun onto the quasi-2D films cast on patterned PEDOT/ITO glass at 1000 rpm for 30 s and 4000 rpm for 30 s, respectively. Afterwards, these films were placed into the vacuum chamber for thermal evaporating of the silver (Ag) electrodes and complete the fabrication of 2D PSCs with the structure of ITO glass/PEDOT: PSS/Quasi-2D perovskite film/PCBM/PEIE/Ag with active area of 0.1 $cm^2$. Current density-Voltage (J-V) curves of 2D PSCs were measured using a Keithley 2400 Source Meter under standard solar illumination (AM 1.5G, 100 $mW \cdot cm^{-2}$) and the stability tests of the encapsulated PSCs in air were conducted using the Candlelight Maximum Power Tracker.

### 2. Film Peeling Methods

*Obtaining the peeling edges*: A piece of scotch tape was adhered to the top surface of the $BA_2MA_{n-1}Pb_nI_{3n+1}$ (<*n*>=5) perovskite films deposited on PEDOT/ITO glass substrate followed by firm manual compression. Afterwards, the tape was peeled off rapidly by hand from one side, leading to the partially peeled quasi-2D film on the PEDOT/ITO glass substrate. The boundaries between the unpeeled film area residue on the substrate and the bare substrate region are defined as the "peeling edges".

*Access to bottom surfaces*: The self-mixing instant epoxy (LOCTITE) was used to fully peel off the quasi-2D perovskite film from the PEDOT/ITO glass substrate. The detailed process is described in the

Results and Discussion section. After peeling, the film was adhered to a new substrate by the solidified epoxy, exposing the previously bottom surface of the quasi-2D film to the air.

**3. Photo-physical Characterisations**

*Transient absorption (TA) spectroscopy*: Femtosecond pump-probe TA measurements of the $BA_2MA_{n-1}Pb_nI_{3n+1}$ (<*n*>=5) quasi-2D perovskite films hot-cast on PEDOT/glass substrates were performed using a TA spectrometer at room temperature. The 800 nm pulsed output (96 kHz, 60 fs FWHM) generated by a high repetition rate amplifier (Coherent RegA 9050) was split to generate the pump (525 nm) beam through a tunable optical parametric amplifier (Coherent OPA 9450) and the probe (visible/near-IR white light) beam using a 3-mm-thick sapphire window (CASTECH), respectively. Pump and probe pulses were focused by an off-axis parabolic reflector to overlap at the surface of the film sample with a pump spot size of ~200 μm, giving an excitation fluence of 1.6 $\mu J \cdot cm^{-2}$. Pump-induced absorption changes (ΔOD) were measured by comparing transmitted probe pulses with and without pump pulses modulated by a synchronised mechanical chopper in the path of the pump beam. The time-resolved transient absorption spectra were recorded using a high-speed fiber-optic spectrometer (Ultrafast Systems). The TA spectra of the quasi-2D perovskite film were collected under both the top-side (air) and bottom-side (glass) excitation (transmitted probe detection) mode.

*PL spectroscopy*: The PL spectra of $BA_2MA_{n-1}Pb_nI_{3n+1}$ (<*n*>=5) quasi-2D perovskite films hot-cast on PEDOT/glass substrates were collected by a scanning confocal microscope (Olympus, IX71/FV300) equipped with a fluorescence spectrometer (Ocean Optics). The 400 nm excitation beam was the frequency-doubled output of a mode-locked and cavity dumped Ti:Sapphire laser (Coherent Mira900f/APE PulseSwitch, 100 fs FWHM), which was focused on either the top (air) or bottom (substrate) side of the films through a 20× objective lens, with the laser intensity of ~0.5 $kW/cm^2$.

**4. Morphological Characterisations**

*AFM*: AFM measurements were performed using a Bruker Dimension Icon (Bruker Corporation, USA) operating in PeakForce Tapping and SoftTapping mode. A combination of sharp silicon nitride probes (Bruker ScanAsyst-Air) and silicon probes (Bruker RTESPA-150) were used. In SoftTapping mode, the instrument was operated at 5-8% below the resonant frequency to minimise force on the surface. In PeakForce tapping mode, a small Peak Force setpoint was used in combination with software-controlled gain to minimise force on the sample surface. Scan rates ranging from 0.25 Hz to 0.5 Hz were used.

*SEM*: A scanning electron microscope (FEI Nova Nanolab 200) was used to obtain the top-view SEM images of the partially peeled $BA_2MA_{n-1}Pb_nI_{3n+1}$ (<*n*>=5) quasi-2D perovskite film on PEDOT/ITO glass and the bottom surface of the quasi-2D film peeled from PEDOT/ITO glass substrate. Secondary electrons are collected to generate the topographic features of the film samples.

**5. Structural Characterisations**

*XRD*: X-ray diffraction pattern of the $BA_2MA_{n-1}Pb_nI_{3n+1}$ (<*n*>=5) quasi-2D perovskite film deposited on PEDOT/glass substrate was obtained using a Rigaku Smart Lab X-ray diffractometer with X-ray wavelength of λ=1.542 Å generated by Cu $K_\alpha$ emission. Bragg-Brentano geometry was adopted for collecting diffraction singles from the out-of-plane direction.

*GI-WAXS*: Both the $BA_2MA_{n-1}Pb_nI_{3n+1}$ (<*n*>=5) quasi-2D perovskite films deposited on PEDOT/ITO substrate (top surface) and those peeled off by epoxy glue (bottom surface) were characterised by GI-WAXS based on the SAXS/WAXS beamline at Australian Synchrotron. The X-ray photon energy is fixed at 15 keV, and the incidence angles are set as 0.1° and 0.3°. Both the samples and the Pilatus 2M CCD detector are placed inside vacuum chambers ($< 1 \times 10^{-5}$ mbar) with a sample to detector distance of 600 mm.

*Simulation of GI-WAXS*: The crystallographic information file (CIF) of $MAPbI_3$ and $BA_2MA_{n-1}Pb_nI_{3n+1}$ (*n*=3, 4) utilised for the GI-WAXS pattern simulation were downloaded from the Crystallography Open Database (http://www.crystallography.net/cod/search.html). Structure factor (SF) files of these crystals are extracted by the VESTA software. Afterwards, the Python script shared by Naveen Raj Venkatesan (https://github.com/venkatesannaveen/xray-scattering-tools) was applied to generate the GI-WAXS patterns of the specifically oriented 3D or 2D perovskite crystals.

## ACKNOWLEDGEMENT

Funding support from the ARC Centre of Excellence in Exciton Science (CE170100026) is acknowledged. T.R., M.G., and D.A. acknowledge the financial support from the Devices & Engineered System Program of CSIRO Manufacturing. C.L., T.A.S., M.G., and D.A. further acknowledge the Australian Centre for Advanced Photovoltaics (ACAP) program funded by the Australian Government through the Australian Renewable Energy Agency (ARENA). The Australian Government does not accept responsibility for the views, information or advice expressed herein. C.H. is the recipient of an Australian Research Council Future Fellowship (FT210100113), funded by the Australian Government. GIWAXs measurements were undertaken on the SAXS/WAXS beamline at the Australian Synchrotron facilities, part of ANSTO.

## ASSOCIATED CONTENT

### *Supporting Information*

The Supporting Information is available free of charge at *****.

Pseudo-colour 2D plot of the TA spectrum of the $BA_2MA_{n-1}Pb_nI_{3n+1}$ (<*n*>=5) quasi-2D perovskite film obtained by bottom-side excitation and transmission detection; UV-vis absorption spectra of the $BA_2MA_{n-1}Pb_nI_{3n+1}$ (<*n*>=5) film; AFM images and height profile analysis of the top surface of the $BA_2MA_{n-1}Pb_nI_{3n+1}$ (<*n*>=5) film; Low magnification SEM image (top-view) of the $BA_2MA_{n-1}Pb_nI_{3n+1}$

(<*n*>=5) film after partially peeling by scotch tape; AFM images of the bottom and top surface morphology of the $BA_2MA_{n-1}Pb_nI_{3n+1}$ (<*n*>=5) film exposed to air for one week; Optical transmission images of the $BA_2MA_{n-1}Pb_nI_{3n+1}$ (<*n*>=5); Simulated GI-WAXS patterns of $MAPbI_3$ (3D) perovskite film with horizontal (<110>) and vertical (<$\bar{1}$10>) crystal orientation; GI-WAXS pattern of the $MAPbI_3$ film (top surface) obtained with an X-ray incidence angle of 0.1°.

# AUTHOR INFORMATION


### *Corresponding Authors*

**Dechan Angmo** − *Devices and Engineered Systems, CSIRO Manufacturing, Clayton, VIC 3168, Australia;* Email: Dechan.Angmo@csiro.au

**Kenneth P. Ghiggino** − *School of Chemistry and ARC Centre of Excellence in Exciton Science, The University of Melbourne, Parkville, Victoria 3010, Australia*; Email: ghiggino@unimelb.edu.au

### *Authors*

**Fei Zheng** − *School of Chemistry and ARC Centre of Excellence in Exciton Science, The University of Melbourne, Parkville, Victoria 3010, Australia; Devices and Engineered Systems, CSIRO Manufacturing, Clayton, VIC 3168, Australia*

**Thomas Raeber** − *Materials Characterization and Modelling, CSIRO Manufacturing, Clayton, VIC 3168, Australia*

**Sergey Rubanov** − *Ian Holmes Imaging Centre, Bio21 Institute, The University of Melbourne, Victoria 3010, Australia*

**Calvin Lee** − *Bio21 Institute and School of Chemistry, University of Melbourne, Parkville, VIC 3010, Australia*

**Aaron Seeber** − *Materials Characterization and Modelling, CSIRO Manufacturing, Clayton, VIC 3168, Australia*

**Christopher Hall** − *School of Chemistry and ARC Centre of Excellence in Exciton Science, The University of Melbourne, Parkville, Victoria 3010, Australia*

**Trevor A. Amith** − *School of Chemistry and ARC Centre of Excellence in Exciton Science, The University of Melbourne, Parkville, Victoria 3010, Australia*

**Mei Gao** − *Devices and Engineered Systems, CSIRO Manufacturing, Clayton, VIC 3168, Australia*


### *Notes*

The authors declare no conflicts of interest.

# REFERENCES

(1) Roy, P.; Kumar Sinha, N.; Tiwari, S.; Khare, A., A Review on Perovskite Solar Cells: Evolution of Architecture, Fabrication Techniques, Commercialization Issues and Status. *Sol. Energy* **2020,** *198*, 665-688.

(2) Green, M. A.; Dunlop, E. D.; Hohl‐Ebinger, J.; Yoshita, M.; Kopidakis, N.; Hao, X., Solar Cell Efficiency Tables (Version 58). *Prog. Photovolt.: Res. Appl. 2021, 29, 657-667*.

(3) Conings, B.; Drijkoningen, J.; Gauquelin, N.; Babayigit, A.; D'Haen, J.; D'Olieslaeger, L.; Ethirajan, A.; Verbeeck, J.; Manca, J.; Mosconi, E.; Angelis, F. D.; Boyen, H.-G., Intrinsic Thermal Instability of Methylammonium Lead Trihalide Perovskite. *Adv. Energy Mater.* **2015,** *5*, 1500477.

(4) Zheng, F.; Chen, W.; Bu, T.; Ghiggino, K. P.; Huang, F.; Cheng, Y.; Tapping, P.; Kee, T. W.; Jia, B.; Wen, X., Triggering the Passivation Effect of Potassium Doping in Mixed-Cation Mixed-Halide Perovskite by Light Illumination. *Adv. Energy Mater.* **2019,** *9* (24), 1901016.

(5) Cao, D. H.; Stoumpos, C. C.; Farha, O. K.; Hupp, J. T.; Kanatzidis, M. G., 2D Homologous Perovskites as Light-Absorbing Materials for Solar Cell Applications. *J. Am. Chem. Soc.* **2015,** *137* (24), 7843-7850.

(6) Xiao, X.; Dai, J.; Fang, Y.; Zhao, J.; Zheng, X.; Tang, S.; Rudd, P. N.; Zeng, X. C.; Huang, J., Suppressed Ion Migration along the In-Plane Direction in Layered Perovskites. *ACS Energy Lett.* **2018,** *3* (3), 684-688.

(7) Huang, W.; Bu, T.; Huang, F.; Cheng, Y.-B., Stabilizing High Efficiency Perovskite Solar Cells with 3D-2D Heterostructures. *Joule* **2020,** *4* (5), 975-979.

(8) Stoumpos, C. C.; Cao, D. H.; Clark, D. J.; Young, J.; Rondinelli, J. M.; Jang, J. I.; Hupp, J. T.; Kanatzidis, M. G., *Ruddlesden*–Popper Hybrid Lead Iodide Perovskite 2D Homologous Semiconductors. *Chem. Mater.* **2016,** *28* (8), 2852-2867.

(9) Tsai, H.; Nie, W.; Blancon, J. C.; Stoumpos, C. C.; Asadpour, R.; Harutyunyan, B.; Neukirch, A. J.; Verduzco, R.; Crochet, J. J.; Tretiak, S.; Pedesseau, L.; Even, J.; Alam, M. A.; Gupta, G.; Lou, J.; Ajayan, P. M.; Bedzyk, M. J.; Kanatzidis, M. G., High-efficiency Two-dimensional Ruddlesden-Popper Perovskite Solar Cells. *Nature* **2016,** *536* (7616), 312-6.

(10) Zhang, F.; Lu, H.; Tong, J.; Berry, J. J.; Beard, M. C.; Zhu, K., Advances in Two-dimensional Organic–Inorganic Hybrid Perovskites. *Energy Environ. Sci.* **2020,** *13* (4), 1154-1186.

(11) Liang, C.; Gu, H.; Xia, Y.; Wang, Z.; Liu, X.; Xia, J.; Zuo, S.; Hu, Y.; Gao, X.; Hui, W.; Chao, L.; Niu, T.; Fang, M.; Lu, H.; Dong, H.; Yu, H.; Chen, S.; Ran, X.; Song, L.; Li, B.; Zhang, J.; Peng, Y.; Shao, G.; Wang, J.; Chen, Y.; Xing, G.; Huang, W., Two-dimensional Ruddlesden–Popper Layered Perovskite Solar Cells Based on Phase-pure Thin Films. *Nat. Energy* **2020,** *6* (1), 38-45.

(12) Wu, G.; Liang, R.; Ge, M.; Sun, G.; Zhang, Y.; Xing, G., Surface Passivation Using 2D Perovskites toward Efficient and Stable Perovskite Solar Cells. *Adv. Mater.* **2022,** *34* (8), e2105635.

(13) Yu, D.; Wei, Q.; Li, H.; Xie, J.; Jiang, X.; Pan, T.; Wang, H.; Pan, M.; Zhou, W.; Liu, W.; Chow, P. C. Y.; Ning, Z., Quasi-2D Bilayer Surface Passivation for High Efficiency Narrow Bandgap Perovskite Solar Cells. *Angew. Chem. Int. Ed.* **2022,** *61* (20), 202202346.

(14) Jang, Y.-W.; Lee, S.; Yeom, K. M.; Jeong, K.; Choi, K.; Choi, M.; Noh, J. H., Intact 2D/3D Halide Junction Perovskite Solar Cells via Solid-phase In-plane Growth. *Nat. Energy* **2021,** *6* (1), 63-71.

(15) Wang, Z.; Lin, Q.; Chmiel, F. P.; Sakai, N.; Herz, L. M.; Snaith, H. J., Efficient Ambient-air-stable Solar Cells with 2D–3D Heterostructured Butylammonium-caesium-formamidinium Lead Halide Perovskites. *Nat. Energy* **2017,** *2* (9).

(16) Chen, P.; Bai, Y.; Wang, S.; Lyu, M.; Yun, J. H.; Wang, L., In Situ Growth of 2D Perovskite Capping Layer for Stable and Efficient Perovskite Solar Cells. *Adv. Funct. Mater.* **2018,** *28* (17).

(17) Zuo, C.; Scully, A. D.; Vak, D.; Tan, W.; Jiao, X.; McNeill, C. R.; Angmo, D.; Ding, L.; Gao, M., Self-Assembled 2D Perovskite Layers for Efficient Printable Solar Cells. *Adv. Energy Mater.* **2019,** *9* (4), 1803258.

(18) Yang, Y.; Liu, C.; Mahata, A.; Li, M.; Roldán-Carmona, C.; Ding, Y.; Arain, Z.; Xu, W.; Yang, Y.; Schouwink, P. A.; Züttel, A.; De Angelis, F.; Dai, S.; Nazeeruddin, M. K., Universal Approach Toward

High-efficiency Two-dimensional Perovskite Solar Cells via a Vertical-rotation Process. *Energy Environ. Sci.* **2020,** *13* (9), 3093-3101.

(19) Quintero-Bermudez, R.; Gold-Parker, A.; Proppe, A. H.; Munir, R.; Yang, Z.; Kelley, S. O.; Amassian, A.; Toney, M. F.; Sargent, E. H., Compositional and Orientational Control in Metal Halide Perovskites of Reduced Dimensionality. *Nat. Mater.* **2018,** *17* (10), 900-907.

(20) Mauck, C. M.; Tisdale, W. A., Excitons in 2D Organic–Inorganic Halide Perovskites. *Trends Chem.* **2019,** *1* (4), 380-393.

(21) Ren, H.; Yu, S.; Chao, L.; Xia, Y.; Sun, Y.; Zuo, S.; Li, F.; Niu, T.; Yang, Y.; Ju, H.; Li, B.; Du, H.; Gao, X.; Zhang, J.; Wang, J.; Zhang, L.; Chen, Y.; Huang, W., Efficient and Stable Ruddlesden–Popper Perovskite Solar Cell with Tailored Interlayer Molecular Interaction. *Nat. Photonics* **2020,** *14* (3), 154-163.

(22) Zhang, F.; Kim, D. H.; Lu, H.; Park, J. S.; Larson, B. W.; Hu, J.; Gao, L.; Xiao, C.; Reid, O. G.; Chen, X.; Zhao, Q.; Ndione, P. F.; Berry, J. J.; You, W.; Walsh, A.; Beard, M. C.; Zhu, K., Enhanced Charge Transport in 2D Perovskites via Fluorination of Organic Cation. *J. Am. Chem. Soc.* **2019,** *141* (14), 5972-5979.

(23) Zheng, F.; Zuo, C.; Niu, M.; Zhou, C.; Bradley, S. J.; Hall, C. R.; Xu, W.; Wen, X.; Hao, X.; Gao, M.; Smith, T. A.; Ghiggino, K. P., Revealing the Role of Methylammonium Chloride for Improving the Performance of 2D Perovskite Solar Cells. *ACS. Appl. Mater. Interfaces* **2020,** *12* (23), 25980-25990.

(24) Soe, C. M. M.; Nie, W.; Stoumpos, C. C.; Tsai, H.; Blancon, J.-C.; Liu, F.; Even, J.; Marks, T. J.; Mohite, A. D.; Kanatzidis, M. G., Understanding Film Formation Morphology and Orientation in High Member 2D Ruddlesden-Popper Perovskites for High-Efficiency Solar Cells. *Adv. Energy Mater.* **2018,** *8* (1), 1700979.

(25) Lai, H.; Lu, D.; Xu, Z.; Zheng, N.; Xie, Z.; Liu, Y., Organic-Salt-Assisted Crystal Growth and Orientation of Quasi-2D Ruddlesden-Popper Perovskites for Solar Cells with Efficiency over 19. *Adv. Mater.* **2020,** *32* (33), 2001470.

(26) Zhou, N.; Zhang, Y.; Huang, Z.; Guo, Z.; Zhu, C.; He, J.; Chen, Q.; Sun, W.; Zhou, H., Mobile Media Promotes Orientation of 2D/3D Hybrid Lead Halide Perovskite for Efficient Solar Cells. *ACS Nano* **2021,** *15* (5), 8350-8362.

(27) Lai, X.; Li, W.; Gu, X.; Chen, H.; Zhang, Y.; Li, G.; Zhang, R.; Fan, D.; He, F.; Zheng, N.; Yu, J.; Chen, R.; Kyaw, A. K. K.; Sun, X. W., High-performance Quasi-2D perovskite solar cells with power conversion efficiency over 20% fabricated in humidity-controlled ambient air. *Chem. Eng. J.* **2022,** *427*, 130949.

(28 Othman, M.; Zheng, F.; Seeber, A.; Chesman, A. S. R.; Scully, A. D.; Ghiggino, K. P.; Gao, M.; Etheridge, J.; Angmo, D., Millimeter‐Sized Clusters of Triple Cation Perovskite Enables Highly Efficient and Reproducible Roll‐to‐Roll Fabricated Inverted Perovskite Solar Cells. *Adv. Funct. Mater.* **2021,** 32, 2110700.

(29) Chen, Y.; Sun, Y.; Peng, J.; Tang, J.; Zheng, K.; Liang, Z., 2D Ruddlesden-Popper Perovskites for Optoelectronics. *Adv. Mater.* **2018,** *30* (2), 1703487.

(30) Xu, Y.; Wang, M.; Lei, Y.; Ci, Z.; Jin, Z., Crystallization Kinetics in 2D Perovskite Solar Cells. *Advanced Energy* Materials **2020,** *10* (43).

(31) Lin, Y.; Fang, Y.; Zhao, J.; Shao, Y.; Stuard, S. J.; Nahid, M. M.; Ade, H.; Wang, Q.; Shield, J. E.; Zhou, N.; Moran, A. M.; Huang, J., Unveiling the operation mechanism of layered perovskite solar cells. *Nat Commun* **2019,** *10* (1), 1008.

(32) Zheng, F.; Hall, C. R.; Angmo, D.; Zuo, C.; Rubanov, S.; Wen, Z.; Bradley, S. J.; Hao, X.-T.; Gao, M.; Smith, T. A.; Ghiggino, K. P., A sandwich-like structural model revealed for quasi-2D perovskite films. *J. Mater. Chem. C* **2021,** *9* (16), 5362-5372.

(33) Quan, L. N.; Yuan, M.; Comin, R.; Voznyy, O.; Beauregard, E. M.; Hoogland, S.; Buin, A.; Kirmani, A. R.; Zhao, K.; Amassian, A.; Kim, D. H.; Sargent, E. H., Ligand-Stabilized Reduced-Dimensionality Perovskites. *J. Am. Chem. Soc.* **2016,** *138* (8), 2649-55.

(34) Liu, J.; Leng, J.; Wu, K.; Zhang, J.; Jin, S., Observation of Internal Photoinduced Electron and Hole Separation in Hybrid Two-Dimentional Perovskite Films. *J. Am. Chem. Soc.* **2017,** *139* (4), 1432-1435.

(35) Zuo, C.; Scully, A. D.; Tan, W. L.; Zheng, F.; Ghiggino, K. P.; Vak, D.; Weerasinghe, H.; McNeill, C. R.; Angmo, D.; Chesman, A. S. R.; Gao, M., Crystallisation Control of Drop-cast Quasi-2D/3D Perovskite Layers for Efficient Solar Cells. *Commun. Mater.* **2020,** *1* (1), 33.

(36) Stoumpos, C. C.; Soe, C. M. M.; Tsai, H.; Nie, W.; Blancon, J.-C.; Cao, D. H.; Liu, F.; Traoré, B.; Katan, C.; Even, J.; Mohite, A. D.; Kanatzidis, M. G., High Members of the 2D Ruddlesden-Popper Halide Perovskites: Synthesis, Optical Properties, and Solar Cells of $(CH_3(CH_2)_3NH_3)_2(CH_3NH_3)_4Pb_5I_{16}$. *Chem* **2017,** *2* (3), 427-440.

(37) Zheng, F.; Angmo, D.; Hall, C. R.; Rubanov, S.; Yuan, F.; Laird, J. S.; Gao, M.; Smith, T. A.; Ghiggino, K. P., Brownian Tree‐Shaped Dendrites in Quasi‐2D Perovskite Films and Their Impact on Photovoltaic Performance. *Adv. Mater. Interfaces* **2022,** *9* (13), 2102231.

(38) Shi, E.; Yuan, B.; Shiring, S. B.; Gao, Y.; Akriti; Guo, Y.; Su, C.; Lai, M.; Yang, P.; Kong, J.; Savoie, B. M.; Yu, Y.; Dou, L., Two-dimensional Halide Perovskite Lateral Epitaxial Heterostructures. *Nature* **2020,** *580* (7805), 614-620.

(39) Akriti; Shi, E.; Shiring, S. B.; Yang, J.; Atencio-Martinez, C. L.; Yuan, B.; Hu, X.; Gao, Y.; Finkenauer, B. P.; Pistone, A. J.; Yu, Y.; Liao, P.; Savoie, B. M.; Dou, L., Layer-by-layer Anionic Diffusion in Two-dimensional Halide Perovskite Vertical Heterostructures. *Nat. Nanotechnol.* **2021,** *16* (5), 584-591.

(40) Ariga, K.; Yamauchi, Y.; Mori, T.; Hill, J. P., 25th Anniversary Article: What Can be Done with The Langmuir-Blodgett Method? Recent Developments and Its Critical Role in Materials science. *Adv. Mater.* **2013,** *25* (45), 6477-512.

(41) Winter, B.; Weber, R.; Schmidt, P. M.; Hertel, I., Molecular Structure of Surface-Active Salt Solutions: Photoelectron Spectroscopy and Molecular Dynamics Simulations of Aqueous Tetrabutylammonium Iodide. *J. Phys. Chem. B* **2004,** *108* (38), 14558-14564.

(42) Chen, S.; Xiao, X.; Chen, B.; Kelly, L. H.; Zhao, J.; Lin, Y.; Toney, M. F.; Huang, J., Crystallization in One-step Solution Deposition of Perovskite Films: Upward or Downward? *Sci. Adv.* **2021,** 7, abb2412.

(43) Chen, S.; Dai, X.; Xu, S.; Jiao, H.; Zhao, L.; Huang, J., Stabilizing Perovskite-substrate Interfaces for High-performance Perovskite Modules. *Science* **2021,** *373*, 902.

(44) Venkatesan, N. Charge-Carrier Dynamics and Structural Characterization of Layered Hybrid Halide Perovskites. Doctoral dissertation, University of California: Santa Barbara, **2020**, eScholarship, https://escholarship.org/uc/item/2kn3j1t3 (Apr. 10, 2022).

(45) Tan, W. L.; McNeill, C. R., X-ray Diffraction of Photovoltaic Perovskites: Principles and Applications. *Appl. Phys. Rev.* **2022,** *9* (2), 021310.

(46) Tan, W. L.; Cheng, Y.-B.; McNeill, C. R., Direct Assessment of Structural Order and Evidence for Stacking Faults in Layered Hybrid Perovskite Films from X-ray Scattering Measurements. *J. Mater. Chem. A* **2020,** *8*, 12790-12798.

(47) Cheng, P.; Wang, P.; Xu, Z.; Jia, X.; Wei, Q.; Yuan, N.; Ding, J.; Li, R.; Zhao, G.; Cheng, Y.; Zhao, K.; Liu, S. F., Ligand-Size Related Dimensionality Control in Metal Halide Perovskites. *ACS Energy Lett.* **2019,** *4* (8), 1830-1838.

(48) Guentert, O. J., Study of the Anomalous Surface Reflection of X Rays. *J. Appl. Phys.* **1965,** *36* (4), 1361-1366.

(49) Venkatesan, N. R.; Labram, J. G.; Chabinyc, M. L., Charge-Carrier Dynamics and Crystalline Texture of Layered Ruddlesden–Popper Hybrid Lead Iodide Perovskite Thin Films. *ACS Energy Lett.* **2018,** *3* (2), 380-386.

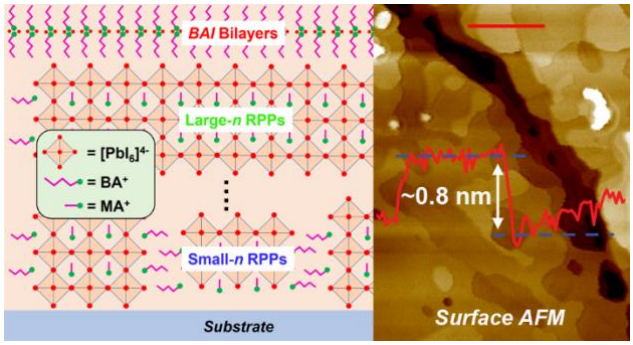


**For Table of Contents Only**